



Characteristics of convective boundary layer and associated entrainment zone as observed by a ground-based polarization lidar

Fuchao Liu^{1,2,3}, Fan Yi^{1,2,3}, Zhenping Yin^{1,2,3}, Yunpeng Zhang^{1,2,3}, Yun He^{1,2,3}, Yang Yi^{1,2,3}

¹School of Electronic Information, Wuhan University, Wuhan, 430072, China

²Key Laboratory of Geospace Environment and Geodesy, Ministry of Education, Wuhan, 430072, China

³State Observatory for Atmospheric Remote Sensing, Wuhan 430072, China

Correspondence to: Fuchao Liu (lfc@whu.edu.cn), Fan Yi (yf@whu.edu.cn)

Abstract

A tilted polarization lidar (TPL) with a pointing angle of 30° off zenith has been developed for continuous monitoring of the atmosphere with 10-s time and 6.5-m height resolution. From lidar-derived aerosol backscatter, instantaneous ABL depths are retrieved by logarithm gradient method (LGM) and Harr wavelet transform method (HWT), while hourly-mean ABL depths by variance method. A new FWHM method utilizing the full width at half maximum (FWHM) of the variance profile of aerosol backscatter ratio (ABR) fluctuations is proposed to determine the entrainment zone thickness (EZT). Both typical winter and summer clear-day observational cases are presented. It is concluded the convective boundary layer (CBL) evolution can be described by four stages. At the formation stage, the hourly-mean CBL depth grew slowly with a positive growth rate of <0.15 km/h. At the growth stage, the hourly-mean CBL depth grew fast with average growth rate of >0.3 km/h. At the quasi-stationary stage, the hourly-mean CBL depth varied little and the corresponding growth rate changed sign with absolute value of <0.15 km/h. At the decay stage, the hourly-mean CBL depth kept decreasing until the layer being re-categorized as a residual layer. The instantaneous CBL depths exhibited different fluctuation magnitudes in the four stages and fluctuations at the growth stage were generally more obvious. The EZT is investigated by the FWHM method. It is found that for the same statistical time interval of 0900-1900 LT, the winter case had smaller mean (*mean*) and standard deviation (*stddev*) of EZT data (a *mean* of 94 m, a *stddev* of 38 m) than those of the summer case (a *mean* of 127 m, a *stddev* of 49 m); besides, the former had respective percentages of 8.5% and 7.5% of EZT falling into the subranges of 0-50 m and >150 m, while the latter had respective percentages of 2.0% and 31% of EZT falling into the same corresponding subranges. Common statistical characteristics also existed for both cases. The growth stage always had the largest *mean* and *stddev* of EZT and the quasi-stationary stage usually the smallest *stddev* of EZT. For all four stages, most EZT values fell into the 50-150 m subrange; the overall percentages of EZT falling into the 50-150 m subrange between 0900 and 1900 LT were 84% and 67% for the winter and summer cases, respectively.



34 **1 Introduction**

35 Monitoring the atmospheric boundary layer (ABL) is of essential importance since the ABL is in direct contact with nearly
36 all terrestrial life on earth (Lammert et al., 2006). The ABL locates at the lower part of the troposphere and subjects to
37 influences of various processes. These processes, including land or water surface exchanges at the bottom and entrainments
38 at the top, govern the transport of heat, momentum, moisture and substances (e.g., aerosols and other constituents) between
39 the ground and the free atmosphere (FA) (Stull, 1988; Pal et al., 2010).

40
41 The depth (or height) of the ABL is a key parameter for parameterization of the ABL, as it determines the available volume
42 for pollutants dispersion and resulting concentrations (Pal et al., 2015; Li et al., 2017; Su et al., 2018; Su et al., 2020), as well
43 as the region dimension in which transport processes can take place. The ABL depth is defined as the interfacial height that
44 separates the ABL and the FA (Stull, 1988). It actually exhibits apparent diurnal evolution following the local surface
45 temperature variation with a magnitude from a few tens of meters to several kilometers (Kong and Yi, 2015). In clear
46 daytime after sunrise, the ABL depth generally increases first as convective activities intensify, then decreases after reaching
47 its maximum in the afternoon when turbulence intensity decays. The convectively-driven ABL is designated as convective
48 boundary layer (CBL). After sunset, the CBL is replaced by stable boundary layer (SBL; or nocturnal boundary layer, NBL)
49 with a much lower depth. Because the convective processes driven by the sensible heat flux at the surface can be reflected by
50 tracer (e.g., water vapor and aerosols) concentration within the CBL and in various atmospheric variables, multiple methods
51 based on tracers and distinct instrumentations have been utilized to determine the CBL depth (Behrendt et al., 2011a; Cimini
52 et al., 2013; Sawyer and Li, 2013). In-situ radiosonde measurement serves as one popular way to derive CBL depth (Seidel
53 et al., 2010; Guo et al., 2019) for its wide distribution all over the world and long observation history which makes it suitable
54 for CBL depth climatology study (Dang et al., 2019) despite of its low temporal resolution (usually 2–4 times per day). From
55 radiosonde profiles of temperature, pressure, humidity and wind, the CBL depth can be retrieved by parcel method
56 (Hennemuth and Lammert, 2006; Seidel et al., 2010), Richardson method (Seibert et al., 2000; Seidel et al., 2010; Zhang et
57 al., 2013), and gradient method (Seidel et al., 2010). Ground-based remote sensing instruments, such as sodar (Helmis et al.,
58 2012), microwave radiometer (Cimini et al., 2013), wind profiling radar (Liu et al., 2019), ceilometer (Zhu, 2018) and lidar,
59 favour continuous monitoring of the CBL depth at a fixed location; space-borne lidar like Cloud-Aerosol Lidar with
60 Orthogonal Polarization (CALIOP), on the other hand, can provide global coverage, but suffers from low signal-noise ratio
61 (SNR) at daytime for CBL measurements (Liu et al., 2015; Zhang et al., 2016; Su et al., 2017). Among these remote sensing
62 techniques, lidar can continuously measure the atmospheric backscatter with high spatial and temporal resolution which thus
63 enables detailed study on the microscale structures in the CBL. Based on the lidar-derived backscatter information from
64 given trace substances (e.g., water vapor and aerosols), the ABL depth can be determined either by process-based variance
65 method (e.g., Lammert et al., 2006; Martucci et al., 2007; Wulfmeyer et al., 2010; Pal et al., 2013; Kong and Yi, 2015), or by
66 vertical-distribution-based method (e.g., the derivative method; the Harr wavelet transform method) (Cohn et al., 2000;



67 Brooks, 2003; Morille et al., 2007; Baars et al., 2008; Pal et al., 2010; Granados-Muñoz et al., 2012; Lewis et al., 2013;
68 Sawyer and Li, 2013; Su et al., 2020).

69

70 Turbulence is a frequent phenomenon in the CBL and turbulent mixing serves as an effective mechanism resulting in
71 homogeneous distribution of scalars (e.g., humidity, aerosols and other constituents) in middle and lower parts of the CBL
72 (Manninen et al., 2018). The middle and lower parts of the CBL characterized by evenly mixing is also called mixing layer
73 (ML). However, near the top area of the CBL, sharp gradient of scalars might appear due to vigorous mixing of overshooting
74 thermals (by updraft) and FA air (by downdraft) (Stull, 1988). This region corresponds to the entrainment zone (EZ).
75 Entrainment processes occurred in the EZ controls the CBL growth and structure, as well as clouds formation and
76 distribution in the CBL (Brooks et al., 2007). Entrainment rate is an important parameter for understanding the fundamental
77 physical entrainment processes; however, this parameter cannot be directly measured but needs to be inferred from other
78 measurement results (Lenschow et al., 1999). The entrainment zone thickness (EZT) provides a possible approach for
79 parameterizing the entrainment rate (Deardorff et al., 1980). The top of EZ can be regarded as the highest height that the
80 thermal within a region reaches (Stull, 1988), while the bottom of EZ is difficult to define and usually taken subjectively as
81 the height where about 5-10% of the air on a horizontal plane has the FA characteristics (e.g., Deardorff et al., 1980; Wilde
82 et al., 1985). The EZT is determined by the top and bottom heights of the EZ and measures the averaged vertical size of the
83 ABL-height fluctuation (Boers et al., 1995). Since small scale processes often become important in the EZ due to high
84 variability of the scalar distribution in these regions, determination of EZT requires monitoring of tracers with very high
85 temporal-spatial resolution in this area. Based on lidar-retrieved high-resolution time series of instantaneous ABL depth, the
86 standard deviation technique (e.g., Davis et al., 1997) and the cumulative frequency distribution method (e.g., Wilde et al.,
87 1985; Flamant et al., 1997; Pal et al., 2010) have been employed to investigate the EZT.

88

89 In this work we present the measurement results of the CBL and associated EZ using a recently-developed titled polarization
90 lidar (TPL). The TPL is housed in a specially-customized working container and capable of operating under various weather
91 conditions (including heavy precipitation). The TPL has an inclined working angle of 30° off zenith and routinely monitors
92 the atmosphere with a time resolution of 10 s and a height resolution of 6.5 m. The equivalent minimum height with full
93 overlap for the TPL is ~ 173 m above ground level (AGL). Thus this TPL provides a possibility to perform detailed study on
94 the ABL. The instrument, methodology, observational results and summary and conclusions are stated successively in
95 following sections.

96 **2 Instrument**

97 The TPL locates in the campus of Wuhan University, Wuhan, China (30.5° N, 114.4° E and 70 m above sea level). Figure 1a
98 shows a schematic optical layout of the lidar system. The lidar transmitter introduces a solid Nd:YAG laser to generate an



99 emission of 70 mJ per pulse at 532 nm with a repetition of 20 Hz. A Brewster polarizer (PR) improves the linear polarization
100 purity of the outgoing laser light before entering the beam expander (BE). The $3\times$ BE compresses the divergence of the laser
101 to be <0.25 mrad. A steerable reflecting mirror (RM) then guides the expanded beam into atmosphere. In the receiver, a
102 Cassergrain telescope collects the atmospheric backscatter. The telescope has a clear aperture of 203.2 mm and a focal length
103 of 2032 mm. The subsequent optics contains an iris, a collimating lens (CL), a half-wavelength plate (HWP), a RM and an
104 interference filter (IF). The iris sets the telescope field of view to be 1.0 mrad. The HWP guarantees the polarization plane of
105 the propagating light beam to be exactly coincident with the receiver polarization analyzer. The IF has a bandwidth of 0.17
106 nm centered at 532 nm and a peak transmittance of 79%. After being filtered by the IF, the parallel and perpendicular
107 polarization light components are detected by two detection channels (designated as the P- and S-channel, respectively). In
108 each of the P- and S-channel, two cubic polarization beam splitters (PBS) are cascaded to reduce crosstalk between the two
109 orthogonal polarization channels; a focusing lens (FL) then focuses the signal light on the photosensitive surface of
110 subsequent photomultiplier tube (PMT); neutral density filters (not shown here) are also added before the FL to avoid
111 saturation of the PMT. Finally, a PC-controlled two-channel transient digitizer (TR20-160, Licel) records the detected
112 signals as raw saved data with a time resolution of 10 s and range resolution of 7.5 m.

113
114 Figure 1b provides a picture of the TPL transmitting-receiving optics. The whole optics is installed on a mechanical tilted
115 platform (TPF) with a fixed elevation angle of 30° . This translates a same angle of the telescope optical axis off zenith.
116 Besides, the TPL system is housed in a specially-customized working container with temperature and humidity control. The
117 working container opens a window on one side that permits the propagating laser beam and atmospheric backscatter to pass
118 through without blocking. The working container enables the TPL to operate under various weather conditions including
119 heavy precipitation.

120
121 The whole transmitting-receiving optics of the TPL has a compact arrangement and the tested minimum range with full
122 overlap is 200 m. Given the 30° tilted angle off zenith, this yields an equivalent height of ~ 173 m AGL. Thus the TPL partly
123 provides a possibility of the depth investigation of shallow CBL and NBL. The channel gain ratio of the TPL was calibrated
124 after its foundation using sky background method (Wang et al., 2009). Specifically, the calibration was performed when the
125 sky was clouded over so that the background sun light could be regarded as totally unpolarized. The gain ratio turned out to
126 be 0.09521 ± 0.00031 . It is further investigated that the lidar-measured molecular volume depolarization $\delta_{v,m}$ in clear areas is
127 0.00780 ± 0.00072 . Considering the theoretical $\delta_{v,m}$ for this TPL should be 0.00364 (Behrendt et al., 2002), the offset value of
128 0.00416 due to depolarization effect of the lidar system is rather small and thus neglected.



129 3 Methodology

130 3.1 Method to determine ABL depth

131 The Licel-recorded raw analog and photon count data are first used to generate a reasonable photon count profile with larger
132 dynamic range based on a developed gluing algorithm (Newsom et al., 2009; Zhang et al., 2014). This glued photon count
133 profile remains a temporal resolution of 10 s and a range resolution of 7.5 m. Simultaneous the obtained P- and S-channel
134 signals, the unpolarized range-square corrected elastic signal X at range R can be reconstructed by:

$$136 X(R) = [N_p(R) + GR \cdot N_s(R)] \cdot R^2 \quad (1)$$

137
138 where subscripts p and s denote P- and S-channel, respectively. N is the background-subtracted photon count signal. The
139 channel gain ratio GR has already been determined as stated before.

140
141 Since the TPL is slantingly-pointed with an angle of 30° off zenith, the range R can be readily converted to corresponding
142 height z by multiplying a factor of $\cos 30^\circ$. Hereafter in this work we use height z instead of range R . From the range-square
143 corrected elastic signal X , the vertical-distribution-based method can be employed to determine an ABL depth for each X
144 profile. Here both the logarithm gradient method (LGM) (e.g., Wulfmeyer, 1999; Pal et al., 2010) and Harr wavelet
145 transform method (HWT) (e.g. Davis et al., 2000; Brooks, 2003) are tested to retrieve ABL depth.

146
147 The ABL depth z_{LGM} determined by LGM method is defined as:

$$149 z_{LGM} = \min[D(z)] = \min\left[\frac{d \ln X(z)}{dz}\right] \quad (2)$$

150
151 where D stands for the derivative of logarithmic X .

152
153 The ABL depth z_{HWT} determined by HWT method is defined as:

$$154 z_{HWT} = \max[W_f(a, b)] = \max\left[\frac{1}{a} \int_{z_{min}}^{z_{max}} X(z) H\left(\frac{z-b}{a}\right) dz\right]$$

155 *for* $z_{min} < b < z_{max}$

$$and H\left(\frac{z-b}{a}\right) = \begin{cases} 1, & b - a/2 \leq z \leq b \\ -1, & b < z \leq b + a/2 \\ 0, & elsewhere \end{cases} \quad (3)$$

156



157 in which W_f is the covariance transform value, H the Harr wavelet function. The dilation a is tested and set to be 200 m for
158 this work. z_{min} and z_{max} are the lower and upper heights for the lidar signal profile, respectively.

159
160 The advantage of applying the LGM and HWT methods is that an instantaneous ABL depth can be determined according to
161 each X profile which favors a high temporal resolution. However, in case of residual layer (RL) or multiple aerosol layers,
162 usually several local minima occur for the retrieved D profile, making the choice of the true minimum for the LGM method
163 difficult (Menut et al., 1999; Pal et al., 2010). As for the HWT method, when the ABL is shallow (e.g., for the NBL and the
164 early stage of the CBL after sunrise), subjective constrain on the upper integral height z_{max} needs to be made to the base of
165 existing aerosol layers aloft (Gan et al., 2011). All these situations hinder the LGM and HWT methods from an automated
166 and robust attribution of the ABL depth.

167
168 To find a more reliable method suitable for an automated procedure, the process-based variance method can be utilized to
169 provide a reference for the search of a local minimum by the LGM method, or the search of a local maximum by the HWT
170 method in a given time interval (e.g., Lammert et al., 2006; Pal et al., 2013). In this work the variance profile of aerosol
171 backscatter ratio (ABR) fluctuations is calculated and the height with maximum variance is assigned as ABL depth. Here the
172 ABR profile is retrieved using Fernald backward iteration method given a fixed lidar ratio (Fernald, 1984; Behrendt et al.,
173 2011b). The fixed lidar ratio is chosen to be 50 sr at 532 nm according to existing measurement results of urban aerosols
174 (e.g., Ansmann et al., 2005; Müller et al., 2007). Typical time interval is 1 h for generating a variance profile. Note this
175 variance method determines a mean ABL depth for the given 1-h time interval. To attribute the instantaneous ABL depth in
176 the same time interval, the height with local minimum/maximum by the LGM/HWT method nearest to the hourly mean ABL
177 depth by the variance method is selected.

178
179 The remaining problem is that several local peaks might also appear for the variance profile in case of multiple (residual)
180 aerosol layers. This problem is settled by visualizing the contour plots of $D(z)$ and $W_f(z)$ to limit a proper height range for
181 variance calculating. As an example, Figure 2 shows the calculated $D(z)$ and $W_f(z)$ in the height range of 0-2.5 km on Jan 31,
182 2020. Sunrise (SR) and sunset (SS) times are marked by thick black dashed lines. As seen in Figure 2, before 1000 local time
183 (LT) multiple (residual) aerosol layers above 0.5 km were clearly indicated by stripes of local minima of $D(z)$ and maxima
184 of $W_f(z)$; besides, advected aerosols above 0.7 km were also discernible after 1930 LT (see also in Figure 4). From Figure 2,
185 it is found that an abundant aerosol layer subsided from around 1.25 km at 0000 LT to about 0.6 km at 1000 LT. This layer
186 definitely leads to misattribution of ABL depth by the automated procedure using the LGM and HWT methods, as well as
187 that by the variance method. By visualizing these contour plots, it is intuitive and convenient to distinguish and locate the
188 above misleading aerosol layers. Then proper upper height limits for applying the variance method can be correctly
189 determined as the real ABL should be below these multiple (residual) aerosol layers aloft. Around 1930 LT after SS, the



190 subsided CBL near 0.6 km should be re-categorized as a RL. Again, the proper upper height limits for applying the variance
191 method shall be set below the RL for the ABL (NBL) depth determination after 1930 LT.

192 **3.2 Method to determine EZT**

193 Since simultaneous measuring of the atmosphere in a large horizontal plane is actually difficult, an equivalent continuous
194 sampling in the time domain at a fixed monitoring site is favored and can be easily performed, given the Taylor's hypothesis
195 of "frozen turbulence" theory (Stull, 1988). Under this assumption and from the retrieved time series of instantaneous ABL
196 depth, the standard deviation technique (e.g., Davis et al., 1997) and the cumulative frequency distribution method (e.g.,
197 Wilde et al., 1985; Flamant et al., 1997; Pal et al., 2010) can be employed to obtain the EZT. However, the values of EZT
198 obtained by these two methods exhibit obvious discrepancies (e.g., Pal et al., 2010). The choice of specific percentage of air
199 having the FA characteristics for the definition of EZ bottom height is rather subjective and seems variable between different
200 researchers. Moreover, considering that variations of ABL depths can result from not only entrainment but also non-
201 turbulent processes (e.g., atmospheric gravity waves and mesoscale variations in ABL structure), the above methods might
202 not really characterize the true EZ (Davis et al., 1997). This situation motivates us to develop a new approach to determine
203 the EZT in this work.

204
205 Let's revisit the definitions of the top and bottom heights of the EZ firstly given by Deardoff et al. (1980) and Wilde et al.
206 (1985) that have respectively 100% and 5-10% of air on a horizontal plane sharing the FA characteristics. It's concluded the
207 top and bottom heights, especially the bottom one, are defined in a statistically averaging manner. Besides, when observed
208 from a perspective of physical process, entrainment mixing of clean FA air and well mixed ML air generally results in
209 significant fluctuations of scalars (e.g., number density of aerosols) in the EZ (see later in Figure 4 and Figure 7). In the
210 absence of clouds and advected aerosols, the fluctuation magnitudes of aerosol number density in the EZ are usually larger
211 than those in the FA and ML. Taking all above into consideration, the variance of ABR fluctuations is utilized here to
212 statistically represent the fluctuations of aerosol number density. Subsequently the full width at half maximum (FWHM) of
213 the variance profile of ABR fluctuations can be employed to define the EZ, as this FWHM records the recent mixing history
214 and quantitatively indicates in which area the larger variations of aerosol number density (ABR) take place. In detail, the
215 height with maximal variance in a variance profile calculated in a given time interval is firstly located as the ABL depth; this
216 is coincident with the definition by the variance method. Then, the upper and lower heights with half value of the maximum
217 variance are searched and defined as the top and bottom heights of EZ, respectively. The EZT is consequently determined by
218 the height interval between the searched top and bottom heights of EZ. This method is designated as FWHM method here.

219
220 As an example, Figure 3 illustrates the FWHM method of using the variance of ABR fluctuations to determine the EZT. In
221 figure 3a, the profile of standard deviation of ABR, $\sigma(\text{ABR})$, is first calculated for a chosen time interval and plotted as thin
222 black line. From this $\sigma(\text{ABR})$ profile, the CBL depth (indicated by the dotted line) is definitely located at the height with



223 maximum $\sigma(\text{ABR})$. For a strong updraft (as is this case) that carries ML air upward into the FA, intense fluctuations occur in
224 the EZ while less-intense fluctuations in the ML and FA. Therefore the corresponding $\sigma(\text{ABR})$ profile exhibits much larger
225 values near the CBL depth, as well as clear-cut steep upper and lower edges on each side of the CBL depth. Then the
226 FWHM of the $\sigma(\text{ABR})$ profile can be directly and easily determined, which further defines the EZ as well as the
227 corresponding EZT (thick vertical line). However, Figure 3a only stands for an ideal situation, while real atmospheric
228 processes are usually much more complex. Figure 3b describes a less-intense updraft case that the lower edge of the $\sigma(\text{ABR})$
229 profile is not clear-cut enough to locate the lower height of the EZ. In this situation, a quadratic polynomial fitting (dashed
230 line) is applied to the lower edge, so that the “contaminating” fluctuations in the ML is removed. Combining the upper edge
231 and the fitted lower edge, the true EZT is determined (thick vertical line). Note that only the clear-cut steep part of the lower
232 edge (nearly overlapping with the fitted line; see Figure 3b) is chosen for fitting and usually a quadratic polynomial function
233 exhibits satisfactory fitting performance. Figure 3c shows a case in the late afternoon when turbulence is decayed and
234 advected aerosols appear at higher heights. Consequently, neither the upper nor the lower edge of the $\sigma(\text{ABR})$ profile is
235 clear-cut enough. Then quadratic polynomial fittings (dashed lines) are applied to both edges to help determine the EZT
236 (thick vertical line). An automated procedure is hence developed to determine the EZT based on this FWHM method.

237 **4 Observational results**

238 In this section two typical ABL measurement results under clear weather conditions are presented. Note the TPL has an
239 equivalent minimum height of ~ 173 m with full overlap, the retrieved results (e.g., ABR) below 173 m shall not be
240 reasonable and discussions are confined only to heights above this value. Before making subsequent physical analysis on the
241 retrieved results, the corresponding conversion of range R to height z is valid under the assumption that the aerosols are
242 horizontally homogeneous in the related horizontal space. To state this issue, the ABR results by this TPL and another co-
243 located vertically-pointing 532-nm polarization lidar (Kong and Yi, 2015) in our lidar site were compared. The comparisons
244 showed that the concurrent ABR profiles by these two lidars always (at least in the ABL region) had nearly identical
245 structures and magnitudes. This convinced the above assumption and the conversion could be made straightforward. Besides,
246 here we focus mainly on the CBL in this work.

247 **4.1 Case study 1 (Jan 31, 2020)**

248 Figure 4 presents a full-day measurement result of the ABL performed in late winter. Figure 4a provides a time-height
249 contour plot (10-s time and 6.5-m height resolution) of ABR on Jan 31, 2020. It is seen that the atmosphere was quite clear
250 in height ranges between 1.7 and 2.5 km, while multiple (residual) aerosol layers were present below 1.7 km until 1400 LT
251 when they were totally “engulfed” by the well-developed CBL. Advected aerosol layers above ~ 0.6 km were also discernible
252 after 1930 LT. In spite of the presence of these aerosol layers aloft, the variance method is first applied to retrieve the hourly
253 mean ABL depth for each 1-h time interval. Before finding a local maximum from the calculated ABR-variance profile, the



254 proper upper and lower height limits are determined by visualizing the corresponding $D(z)$ and $W_j(z)$ contour plots (see
255 Figure 2). Then the height with local maximal variance between the chosen upper and lower heights is searched and located
256 as the ABL depth (red solid circles). SR and SS times are indicated by thick black dashed lines. As shown by Figure 4a, the
257 values of ABR in the CBL had a direct “response” to the development of CBL depth: between ~ 1030 and 1130 LT when the
258 initial CBL was shallow (CBL depth < 0.35 km), the ABR had larger values reaching 10; then as the CBL depth increased
259 and reached to a maximum of ~ 1.02 km around 1330 LT, the ABR values in the CBL generally decreased. If we assume that
260 in the lidar-observation time interval the probed aerosols didn't undergo chemical and physical reactions, then the change in
261 ABR values can be regarded to the change of aerosol number density in the CBL (Engelmann et al., 2007; Pal et al., 2010).
262 Figure 4a graphically describes the vertical transport of aerosols from surface to upper heights: as the available dispersion
263 volume (CBL depth) enlarges, the ABR values (the mixed aerosol number density) fall. Between 1330 and 1830 LT, the
264 ABR values in the CBL exhibited features of vertical homogeneity (see Figure 4b), indicating the fully mixing of aerosols in
265 the ML.

266
267 Figure 4b over-plots the ABR profiles (thin black lines) in each 1-h time interval. The hourly mean ABR profile is also
268 added (blue line). It is found that the fluctuation features of the over-plotted ABR profiles differ at distinct developing stages
269 of the CBL. In the time interval between ~ 0830 and 1130 LT, the hourly mean CBL depth grew slowly from ~ 0.18 km at
270 around 0830 LT to ~ 0.35 km at around 1130 LT; meanwhile, fluctuations of the over-plotted ABR profiles increased in this
271 initial CBL. This stage corresponds to the formation period of the CBL. After SR, the sun started to heat the surface.
272 Consequently convective activities started to occur and CBL began to develop, but the CBL depth growth was restricted by
273 the upper stable NBL (Stull, 1988). Then the hourly mean CBL depth increased rapidly from ~ 0.35 km at around 1130 LT to
274 ~ 1.02 km at around 1330 LT; fluctuations of the over-plotted ABR profiles kept increasing at first throughout the CBL, then
275 decreased and tended to become uniform in the middle and lower parts of the CBL. This stage denotes the rapid growth
276 period of the CBL. After ~ 1130 LT the cool NBL air was warmed to a temperature near that of the above RL, and the CBL
277 top had reached the base of the RL. At this point the stable NBL capping the CBL vanished, so that thermals could penetrate
278 upward quickly, allowing the growth of the CBL depth with a larger growth rate. However, this rapid growth did not
279 continue after the CBL depth reached the top of the RL, where the FA above prevented thermals from further vertical motion
280 (Stull, 1988). Accompanying the initial penetrating thermals upward, aerosols (as well as other constituents) were
281 transported vertically and turbulently mixed, exhibiting a high fluctuation feature for the ABR in the CBL; while as vertical
282 transport and turbulent mixing continued, aerosols shall be fully mixed in a larger available volume, reflected by both
283 smaller fluctuations of the ABR profiles and values of ABR themselves. Next, the hourly mean CBL depth changed very little
284 from ~ 1.02 km at around 1330 LT to ~ 0.96 km at around 1630 LT; fluctuations of the over-plotted ABR profiles kept
285 decreasing until all the ABR profiles became uniformly upright below the top area of the CBL. This stage represents the
286 quasi-stationary period of the CBL. The little change of the CBL depth is governed by the balance between entrainment and
287 subsidence (Stull, 1988). In this stage, the aerosols had been fully and evenly mixed in the ML, indicated by the smallest



288 fluctuations of the ABR profiles and values of ABR. Finally in the late afternoon, the hourly mean ABL depth maintained
289 decreasing from ~ 0.96 km at around 1630 LT to ~ 0.39 km at around 1930 LT; fluctuations of the over-plotted ABR profiles
290 increased slightly in the ML. This stage describes the decay period of the CBL. As the solar radiation weakened, the strength
291 of convective turbulence reduced so that turbulence could not be maintained against dissipation (Nieuwstadt et al., 1986).
292 The small increase in ABR fluctuations reflected that the decay turbulence could no longer preserve the homogeneous
293 distributions of the aerosols in the ML. After SS the turbulence in the ML might decay completely, then the layer needed to
294 be re-categorized as a RL while at the same time NBL had already formed near surface. It should be noted that for all the
295 four stages, obvious fluctuations of the over-plotted ABR profiles were always present near the top area of the CBL. This
296 fluctuating behavior looked like a “node”, representing the structure of the EZ between the CBL and FA (Kong and Yi,
297 2015).

298
299 Figure 5 investigates further the evolution of the CBL depth on Jan 31, 2020. Figure 5a plots the instantaneous CBL depths
300 (blue) obtained by LGM method (before 1000 and after 1900 LT) and HWT method (between 1000 and 1900 LT). For
301 comparison, the hourly mean ABL depths (red solid circles) by variance method are added. Figure 5b shows the
302 corresponding hourly mean ABL depth growth rate. At the formation stage, the CBL depth growth rate changed sign from
303 negative to positive at ~ 0830 LT and reached a maximum of ~ 0.084 km/h at around 1000 LT. After SR, the ABL depth did
304 not increase immediately until later (the growth rate be negative before ~ 0830 LT). The time interval between SR and 1130
305 LT is roughly defined as the early morning transition (EMT) period (Pal et al., 2010). During this EMT period, the
306 instantaneous CBL depth generally exhibited small deviation from that indicated by the hourly mean ABL depth (red line).
307 At the growth stage, the CBL depth increased with a mean growth rate of > 0.3 km/h and a maximum growth rate of ~ 0.36
308 km/h at around 1200 LT. Meanwhile, the instantaneous CBL depths showed obvious larger deviations and fluctuations. At
309 the quasi-stationary stage, the CBL depth growth rate changed sign at around 1430 LT and varied between 0.09 and -0.12
310 km/h. The accompanying instantaneous CBL depths had comparatively moderate deviations and fluctuations. At the final
311 decay stage, the ABL depth growth rate kept negative with a minimum of -0.40 km/h at around 1900 LT. The fluctuations of
312 instantaneous CBL depth were generally moderate before SS. The ABL depth growth rate returned to nearly zero at ~ 2000
313 LT and the time interval between SS and 2000 LT is roughly defined as the early evening transition (EET) period (Pal et al.,
314 2010). During this EET period, the instantaneous ABL depth exhibited small deviation from that indicated by the hourly
315 mean ABL depth (red line).

316
317 It is visually observable that the time series of instantaneous CBL depth fluctuate on small time scales (Figure 5a), especially
318 in the growth stage, reflecting the entrainment characteristics in the EZ. As already mentioned before, the EZT serves as a
319 measure of averaged vertical size of the ABL-depth fluctuation (Boers et al., 1995). Hence the EZT is calculated and
320 investigated here. Figure 6a plots the CBL depth Z_{CBL} (red) obtained by the variance method between 0900 and 1900 LT
321 on Jan 31, 2020. The EZ upper height Z_{Upper} (magenta) and lower height Z_{Lower} (blue) are determined from the FWHM



322 of the $\sigma(\text{ABR})$ profile (see Figure 3). To generate one $\sigma(\text{ABR})$ profile, a group of 18 consecutive ABR profiles in a time
323 interval of 3 min is utilized. So that the retrieved Z_{CBL} and EZT represent the corresponding mean values in each given
324 time interval of 3 min. Here the choice of 3 min is a compromise between time resolution of EZT and reliability of $\sigma(\text{ABR})$
325 profile. Figure 6b exhibits the resulting EZT (red) and ratio of EZT to Z_{CBL} (blue; for convenience, the ratio is multiplied
326 by a factor of 0.5 so that the two vertical axes share the same scaling range). The overall EZT time series between 0900 and
327 1900 LT had a minimum (*min*) of 26 m, a maximum (*max*) of 267 m and a mean (*mean*) of 94 m with a standard deviation
328 (*stddev*) of 38 m. The ratio values spanned a range from 3.5% to 76.8%. Larger ratio values (>30%) mainly appeared in the
329 formation stage and first half of growth stage of the CBL (before 1230 LT), while most ratio values were <20% after the
330 second half of the growth stage (after 1230 LT).

331
332 Table 1 summarizes the corresponding statistical data for all the four developing stages of the CBL on Jan 31, 2020. It is
333 found that the growth stage had largest EZT statistical data (a *min* of 65 m, a *max* of 267 m, a *mean* of 122 m and a *stddev* of
334 41 m). On the contrary, the quasi-stationary stage exhibited lower EZT statistical data (a *max* of 154 m, a *mean* of 82 m and
335 a *stddev* of 28 m except for a *min* of 39 m). The formation stage (a *min* of 33 m, a *max* of 158 m, a *mean* of 85 m and a
336 *stddev* of 36 m) and decay stage (a *min* of 26 m, a *max* of 180 m, a *mean* of 95 m and a *stddev* of 36m) generally showed
337 comparable statistics of EZT. When the values of EZT are divided into five subranges (see Table 1 for detail), it is observed
338 that the formation stage had a highest percentage of 16.0% of EZT falling into the 0-50 m subrange, while the growth stage
339 had none falling into the same subrange. However, the growth stage had the largest percentage of 17.5% of EZT falling into
340 the 150-200 m subrange, and was the unique stage having EZT value exceeding 200 m. The quasi-stationary stage had the
341 smallest percentage of 1.7% of EZT falling into the 150-200 m subrange. For all four stages, the EZT values mostly fell into
342 the 50-100 m and 100-150 m subranges with corresponding cumulative percentages of 80.0%, 80.0%, 88.3% and 86.0%,
343 respectively.

344 4.2 Case study 2 (May 19, 2020)

345 Figure 7 presents a full-day measurement result of the ABL executed in early summer. Figure 7a provides the time-height
346 contour plot (10 s and 6.5 m resolution) of ABR on May 19, 2020. On this summer day, there were less abundant aerosols
347 above 0.6 km compared to that below 0.6 km between 0000 and 1200 LT. Another advected aerosol layer starting at around
348 0900 LT (not indicated here) above 1.5 km subsided but did not interfere with the lower ABL. The variance method is first
349 used to determine the hourly mean ABL depth for each 1-h time interval (red solid circle). The ABR before 1030 LT showed
350 large values (>8) in the initial CBL below 0.4 km. Then as the CBL depth (red line) increased and reached to a maximal of
351 ~1.15 km at around 1430 LT, the ABR values in the CBL exhibited a decrease below 0.4 km while an general increase
352 between 0.4 km and 1.0 km, indicating the turbulent transport of aerosols from surface to upper heights. Figure 7b over-plots
353 the ABR profiles (thin black lines) in each 1-h time interval and the hourly mean ABR profile (blue line). In the formation
354 period of the CBL, the hourly mean CBL depth grew slowly from ~0.18 km at around 0830 LT to ~0.56 km at around 1230



355 LT; fluctuations of the over-plotted ABR profiles prevailed throughout the CBL. Then in the growth period of the CBL, the
356 hourly mean CBL depth increased rapidly from ~0.56 km at around 1230 LT to ~1.63 km at around 1430 LT; observable
357 fluctuations of the over-plotted ABR profiles continued, but tended to decrease and become uniform in the middle part of
358 CBL. Next in the quasi-stationary period of the CBL, the hourly mean CBL depth changed very little from ~1.63 km at
359 around 1430 LT to ~1.52 km at around 1630 LT; fluctuations of the over-plotted ABR profiles decreased slightly and all the
360 ABR profiles became uniformly upright in the middle part of the CBL. Finally in the decay period of the CBL, the hourly
361 mean ABL depth kept decreasing from ~1.52 km at around 1630 LT to ~0.24 km at around 2030 LT; both fluctuations of the
362 over-plotted ABR profiles and ABR values exhibited small decrease in the middle and lower part of the CBL. Again for all
363 the four periods, obvious fluctuations of the over-plotted ABR profiles were always present near the top area of the CBL.

364

365 Figure 8a plots the instantaneous CBL depth (blue) obtained by LGM method (before 0900 and after 2000 LT) and HWT
366 method (between 0900 and 2000 LT). The hourly mean ABL depths (red solid circles) by variance method are added. Figure
367 8b shows the hourly mean ABL depth growth rate (red solid circles). At the formation stage, the CBL depth growth rate
368 changed sign from negative to positive at ~0800 LT and reached a maximal of ~0.14 km/h at around 0900 LT. The EMT
369 period is roughly defined between SR and 1200 LT. The instantaneous CBL depths exhibited small deviation from that
370 indicated by the hourly mean ABL depth (red line) before 1000 LT, but showed increased deviation later on. At the growth
371 stage, the CBL depth increased with a mean growth rate of > 0.48 km/h and a maximum growth rate of ~0.59 km/h at around
372 1300 LT; meanwhile, the deviations and fluctuations of the instantaneous CBL depths obviously enlarged. At the quasi-
373 stationary stage, the CBL depth growth rate changed sign to be negative at around 1500 LT and varied between -0.04 and -
374 0.07 km/h; the fluctuations of the instantaneous CBL depth remained obvious. At the final decay stage, the ABL depth
375 growth rate kept negative with a minimum of -0.58 km/h at around 2000 LT; the fluctuations of instantaneous ABL depth
376 were still observable. The ABL depth growth rate returned to nearly zero at ~2100 LT and the time interval between SS and
377 2100 LT is roughly defined as the EET period. During the EET period, the instantaneous ABL depth generally exhibited
378 small deviation from that indicated by the hourly mean ABL depth (red line). Note that after SS the CBL should be re-
379 categorized as a RL.

380

381 Figure 9a plots the CBL depth Z_{CBL} (red) obtained by the variance method between 0900 and 1900 LT on May 19, 2020,
382 as well as the EZ upper height Z_{Upper} (magenta) and lower height Z_{Lower} (blue) derived from the FWHM of the $\sigma(\text{ABR})$
383 profile. Figure 9b shows the resulting EZT (red) and ratio of EZT to Z_{CBL} (blue). The overall EZT time series between
384 0900 and 1900 LT had a min of 42 m, a max of 331 m and a mean of 127 m with a stddev of 49 m. The ratio values varied
385 between 4.2% and 66.2%. Larger ratio values (>30%) mainly occurred in the formation stage and the initial of growth stage
386 of the CBL (before 1315 LT), while most ratio values were <20% later on (after 1315 LT).

387



388 Table 2 concludes the corresponding statistics for all the four developing stages of the CBL on May 19, 2020. It can be seen
389 that the growth stage had the largest *mean* (153 m) of EZT, while the formation stage exhibited the lowest *mean* (106 m) of
390 EZT. Besides, the growth stage and quasi-stationary stage had the largest *stddev* (57 m) and the smallest *stddev* (35 m) of
391 EZT, respectively. When the values of EZT are divided into five subranges (see Table 2 for detail), it is found that the
392 formation stage had a percentage of 5.7% of EZT falling into the 0-50 m subrange, while the other three stages had none
393 falling into the same subrange. For this summer case, all four stages had percentages of >15% of EZT falling into the 150-
394 200 m subrange, and the growth stage exhibited the largest percentage of 20.0% of EZT exceeding 200 m. Again for all four
395 stages, the EZT had values mostly falling into the range between 50 and 150 m with corresponding percentages of 75.7%,
396 52.5%, 75% and 60.0%, respectively.

397
398 Table 3 compares the EZT statistics for the winter and summer cases. As shown in Table 3, the two cases exhibited apparent
399 statistical differences. For the same time interval of 0900-1900 LT, the winter case (case 1) had overall statistical EZT data
400 (a *mean* of 94 m, a *stddev* of 38 m) smaller than those of the summer case (case 2; a *mean* of 127 m, a *stddev* of 49 m). Note
401 this statistical conclusion was also true for each of the four developing stages. Besides, the former case had respective
402 percentages of 8.5% and 7.5 % of EZT falling into the subranges of 0-50 m and >150 m, while the latter case had respective
403 percentages of 2.0% and 31 % of EZT falling into the same corresponding subranges. The reason of larger statistical EZT
404 data (*mean* and *stddev*) and higher percentage (possibility) of larger EZT values (>150 m) for the latter case is attributed to
405 the stronger solar radiation reaching earth surface in summer than in winter. Stronger solar radiation generally results in
406 more vigorous and frequent thermals overshooting to higher heights (updrafts) and then moving back (downdrafts).
407 Consequently entrainments take place in larger vertical regions. Hence both the statistical EZT data (*mean* and *stddev*) and
408 possibility of larger EZT value seem to provide measures of entrainment intensity. There were also common statistical
409 characteristics for the two observational cases. For example, the growth stage always had the largest *mean* and *stddev* of
410 EZT; as neither the NBL nor the FA restricts the booming development of the CBL in the growth stage, the entrainments
411 were allowed to occur in a wider vertical range. Besides, the quasi-stationary stage usually had the smallest *stddev* of EZT;
412 this quantitatively reflected the fact that the CBL depth and the EZT changed little in this stage. For all four stages, most
413 EZT values fell into the 50-150 m subrange; the corresponding overall percentages of EZT falling into the 50-150 m
414 subrange between 0900 and 1900 LT were 84% and 67% for the winter and summer cases, respectively.

415 5 Summary and Conclusions

416 A tiled polarization lidar (TPL) has been recently developed for full-day monitoring of the atmospheric boundary layer
417 (ABL) under various weather conditions. The TPL has a pointing angle of 30° off zenith and routinely operates with a time
418 resolution of 10 s and a range (height) resolution of 7.5 (6.5) m. The equivalent minimum height with full overlap for the



419 TPL is ~173 m above ground level (AGL). Thus this TPL partly provides a possibility of the depth investigation of shallow
420 convective boundary layer (CBL) and nocturnal boundary layer (NBL).

421

422 From the lidar-recorded range-square corrected elastic signal X , the two vertical-distribution-based methods (logarithm
423 gradient method, LGM; Harr wavelet transform method, HWT) are tested to retrieve instantaneous ABL depth for each X
424 profile. Before applying the LGM and HWT methods, the process-based variance method is first used to locate the hourly-
425 mean ABL depth. For each given 1-h time interval, the height with maximum variance in the variance profile of aerosol
426 backscatter ratio (ABR) fluctuations is searched as the hourly-mean ABL depth. By visualizing the time-height contour plots
427 of $D(z)$ (defined as derivative of logarithmic X) and $W_f(z)$ (defined as covariance transform value of X), the proper upper
428 height limits needed for choosing the true height with local maximum variance are intuitive and convenient to be correctly
429 determined as the base of the misleading aerosol layers aloft. Then the hourly-mean ABL depths provide a guide for an
430 automated attribution of instantaneous ABL depth by the LGM and HWT methods. A new approach utilizing the full width
431 at half maximum (FWHM) of the variance profile of ABR fluctuations is developed and proposed to determine the
432 entrainment zone thickness (EZT). This new approach is designated as FWHM method in this work.

433

434 Both a winter and a summer cases of the TPL clear-day measurement results of the CBL and associated entrainment zone
435 (EZ) are presented. It is concluded that for both typical cases the CBL depth evolution can be described by four consecutive
436 stages. At the formation stage, the hourly-mean CBL depth grew slowly with a positive growth rate of <0.15 km/h. At the
437 growth stage, the hourly-mean CBL depth grew fast; the hourly-mean CBL depth growth rate was always >0.3 km/h, and
438 could reach a value of 0.59 km/h for the summer case. At the quasi-stationary stage, the hourly-mean CBL depth varied
439 slightly; the hourly-mean CBL depth growth rate changed sign from positive to negative, with absolute value of <0.15 km/h.
440 At the decay stage, the hourly-mean CBL depth kept decreasing; the hourly-mean ABL depth growth rate could be <-0.4
441 km/h after sunset. The instantaneous CBL depths exhibited different fluctuation magnitudes in the four stages and the growth
442 stage always had more obvious fluctuations. The fluctuations of over-plotted ABR profiles in each 1-h time interval also
443 showed different behaviors at respective stages: the fluctuations usually enlarged at the formation stage, while generally
444 decreased in the middle part of the CBL at the late growth and quasi-stationary stages. However, the fluctuations of over-
445 plotted ABR profiles were always prevailing near the top area of the CBL, reflecting the structures of the EZ. The EZT is
446 subsequently investigated in detail by the proposed FWHM method. It is found that for the same statistical time interval of
447 0900-1900 LT, the winter case had smaller mean (*mean*) and standard deviation (*stddev*) of EZT data (a *mean* of 94 m, a
448 *stddev* of 38 m) than those of the summer case (a *mean* of 127 m, a *stddev* of 49 m); besides, the winter case had respective
449 percentages of 8.5% and 7.5 % of EZT values falling into the subranges of 0-50 m and >150 m, while the summer case had
450 respective percentages of 2.0% and 31 % of EZT falling into the same corresponding subranges. Common statistical
451 characteristics also existed for both cases. The growth stage always had the largest *mean* and *stddev* of EZT and the quasi-
452 stationary stage usually had the smallest *stddev* of EZT. For all four stages, most EZT values fell into the 50-150 m subrange.



453 The corresponding overall percentages of EZT falling into the 50-150 m subrange between 0900 and 1900 LT are 84% and
454 67% for the winter and summer cases, respectively.

455

456 The proposed FWHM method utilizes the FWHM of the variance profile of the ABR fluctuations to quantify the EZT.
457 Considering the observed ratios of EZT to CBL depth mostly have values of <20%, the retrieved EZT values seem
458 reasonable. In future, this method can be verified by comparisons with other approaches (e.g., comparisons with results by
459 intensive radiosonde). It is also checked that similar characteristics of the four-stage evolution of the CBL and the common
460 statistics of the associated EZ seem to hold true for other 4 clear-day observations. However, it can be much more
461 complicated when heavy aerosol loads and clouds are present. Further investigations on the CBL and EZ under various
462 weather conditions shall be presented in our following works.

463 **Author contributions**

464 FL built the lidar system, performed the data analysis and wrote the initial manuscript. FY conceived the project and led the
465 study. ZY, YZ, YH and YY performed the lidar observations, glued the raw data and participated in scientific discussions.
466 All authors discussed the results and finalized the manuscript.

467 **Competing interests**

468 The authors declare that they have no conflict of interest.

469 **Data availability**

470 Lidar data used in this work are available under permission (yf@whu.edu.cn).

471 **Acknowledgments**

472 This work was funded by the National Natural Science Foundation of China under Grant 41927804. The authors would like
473 to express thanks to Yifan Zhan for discussions on ABL depth retrieving algorithms and to Xiangliang Pan and Wei Wang
474 for lidar calibration experiments and data collections.

475 **References**

476 Baars, H., Ansmann, A., Engelmann, R., and Althausen, D.: Continuous monitoring of the boundary-layer top with lidar,
477 Atmos. Chem. Phys., 8, 7281-7296, doi:10.5194/acpd-8-10749-2008, 2008.



- 478
479 Behrendt, A. and Nakamura, T.: Calculation of the calibration constant of polarization lidar and its dependency on
480 atmospheric temperature, *Opt. Express*, 10, 805-817, doi:10.1364/OE.10.000805, 2002.
- 481
482 Behrendt, A., Pal, S., Aoshima, F., et al.: Observation of convection initiation processes with a suite of state-of-the-art
483 research instruments during COPS IOP 8b, *Q. J. R. Meteorol. Soc.*, 137, 81–100, doi:10.1002/qj.758, 2011a.
- 484
485 Behrendt, A., Pal, S., Wulfmeyer, V., Valdebenito B, Á. M., and Lammel, G.: A novel approach for the characterization of
486 transport and optical properties of aerosol particles near sources-Part I: Measurement of particle backscatter coefficient maps
487 with a scanning UV lidar, *Atmos. Environ.*, 45, 2795-2802, doi:10.1016/j.atmosenv.2011.02.061, 2011b.
- 488
489 Boers, R., Melfi, S. H., and Palm, S. P.: Fractal nature of the planetary boundary layer depth in the trade wind cumulus
490 regime, *Geophys. Res. Lett.*, 22(13), 1705-1708, doi:10.1029/95GL01655, 1995.
- 491
492 Brooks, I. M.: Finding boundary layer top: Application of a wavelet covariance transform to lidar backscatter profiles, *J.*
493 *Atmos. Oceanic Technol.*, 20, 1092-1105, doi:10.1175/1520-0426(2003)020<1092:FBLTAO>2.0.CO;2, 2003.
- 494
495 Brooks, I. M. and Fowler, A. M.: A new measure of entrainment zone structure, *Geophys. Res. Lett.*, 34, L16808,
496 doi:10.1029/2007GL030958, 2007.
- 497
498 Cimini, D., Angelis, F. De, Dupont, J. C., Pal, S., and Haeffelin, M.: Mixing layer height retrievals by multichannel
499 microwave radiometer observations, *Atmos. Meas. Tech.*, 6, 2941–2951, doi:10.5194/amt-6-2941-2013, 2013.
- 500
501 Cohn, S. A. and Angevine, W. M.: Boundary layer height and entrainment zone thickness measured by lidars and wind-
502 profiling radars, *J. Appl. Meteorol.*, 39, 1233-1247, doi:10.1175/1520-0450(2000)0392.0.CO;2, 2000.
- 503
504 Dang, R., Yang, Yi., Hu, X., Wang, Z., and Zhang, S.: A review of techniques for diagnosing the atmospheric boundary
505 layer height (ABLH) using aerosol lidar data, *Remote Sens.*, 11(1590), 1-28, doi:10.3390/rs11131590, 2019.
- 506
507 Deardorff, J. W., Willis, G. E., and Stockton, B. H.: Laboratory studies of the entrainment-zone of a convectively mixed
508 layer, *J. Fluid. Mech.*, 100, 41-64, doi:10.1017/S0022112080001000, 1980.
- 509
510 Davis, K. J., Lenschow, D. H., Oncley, S. P., Kiemle, C., Ehret, G., and Giez, A.: Role of entrainment in surface–atmosphere
511 interactions over a boreal forest, *J. Geophys. Res.*, 102(29), 29218-29230, doi:10.1029/97JD02236, 1997.



- 512
- 513 Davis, K. J., Gamage, N., Hagelberg, C. R., Kiemle, C., Lenschow, D. H., and Sullivan, P. P.: An objective method for
514 deriving atmospheric structure from airborne lidar observations, *J. Atmos. Ocean. Technol.*, 17, 1455–1468,
515 doi:10.1175/1520-0426(2000)0172.0.CO;2, 2000.
- 516
- 517 Engelmann, R., Wandinger, U., Ansmann, A., Müller, D., Žeromskis, E., Althausen, D., and Wehner B.: Lidar Observations
518 of the Vertical Aerosol Flux in the Planetary Boundary Layer, *J. Atmos. Oceanic Technol.*, 25, 1296–1306,
519 doi:10.1175/2007jtecha967.1, 2008.
- 520
- 521 Fernald, F. G.: Analysis of atmospheric lidar observations: Some comments, *Appl. Opt.*, 23, 652–653,
522 doi:10.1364/AO.23.000652, 1984.
- 523
- 524 Flamant, C., Pelon, J., Flamant, P., and Durand, P.: Lidar determination of the entrainment-zone thickness at the top of the
525 unstable marine atmospheric boundary layer, *Boundary-Layer Meteorol.*, 83, 247–284, doi:10.1023/A:1000258318944, 1997.
- 526
- 527 Gan, C. M., Wu, Y., Madhavan, B. L., Gross, B., and Moshary, F.: Application of active optical sensors to probe the vertical
528 structure of the urban boundary layer and assess anomalies in air quality model PM_{2.5} forecasts, *Atmos. Environ.*, 45, 6613–
529 6621, doi:10.1016/j.atmosenv.2011.09.013, 2011.
- 530
- 531 Guo, J., Li, Y., Cohen, J. B., Li, J., Chen, D., Xu, H., Liu, L., Yin, J., Hu, K., and Zhai, P.: Shift in the temporal trend of
532 boundary layer height in China using long-term (1979–2016) radiosonde data, *Geophys. Res. Lett.*, 46, 6080–6089,
533 doi:10.1029/2019GL082666, 2019.
- 534
- 535 Granados-Muñoz, M. J., Navas-Guzmán, F., Bravo-Aranda, J. A., Guerrero-Rascado, J. L., Lyamani, H., Fernández-Gálvez
536 J., and Alados-Arboledas, L.: Automatic determination of the planetary boundary layer height using lidar: One year analysis
537 over southeastern Spain, *J. Geophys. Res.*, 117, D18208, doi:10.1029/2012JD017524, 2012.
- 538
- 539 Helmis, C.G., Sgouros, G., Tombrou, M., Schäfer, K., Münkler, C., Bossioli, E., and Dandou, A. A.: Comparative study and
540 evaluation of mixing-height estimation based on sodar-RASS, ceilometer data and numerical model simulations, *Bound.*
541 *Layer. Meteorol.*, 145, 507–526, doi: 10.1007/s10546-012-9743-4, 2012.
- 542
- 543 Hennemuth, B., and Lammert, A.: Determination of the atmospheric boundary layer height from radiosonde and lidar
544 backscatter, *Boundary Layer Meteorol.*, 120, 181–200, doi:10.1007/s10546-005-9035-3, 2006.
- 545



- 546 Kong, W. and Yi, F.: Convective boundary layer evolution from lidar backscatter and its relationship with surface aerosol
547 concentration at a location of a central China megacity, *J. Geophys. Res. Atmos.*, 120, 7928-7940,
548 doi:10.1002/2015JD023248, 2015.
- 549
- 550 Lammert, A. and Bösenberg, J.: Determination of the convective boundary-layer height with laser remote sensing, *Boundary*
551 *Layer Meteorol.*, 119, 159-170, doi:10.1007/s10546-005-9020-x, 2006.
- 552
- 553 Lenschow, D. H., Krummel, P. B., and Siems, S. T.: Measuring entrainment, divergence, and vorticity on the mesoscale
554 from aircraft, *J. Atmos. Oceanic Technol.*, 16, 1384-1400, doi:10.1175/1520-0426(1999)016<1384:CO;2>, 1999.
- 555
- 556 Lewis, J., Welton, E. J., Molod, A. M., and Joseph, E.: Improved boundary layer depth retrievals from MPLNET, *J. Geophys.*
557 *Res. Atmos.*, 118, 9870-9879, doi:10.1002/jgrd.50570, 2013.
- 558
- 559 Li, Z., Guo, J., Ding, A., Liao, H., Liu, J., Sun, Y., Wang, T., Xue, H., Zhang, H., and Zhu, B.: Aerosol and boundary-layer
560 interactions and impact on air quality, *National Science Review*, 4, 810–833, doi:10.1093/nsr/nwx117, 2017.
- 561
- 562 Liu, B., Ma, Y., Guo, J., Gong, W., Zhang, Y., Mao, F., Li, J., Guo, X., and Shi, Y.: Boundary layer heights as derived from
563 ground-based Radar wind profiler in Beijing, *IEEE T. Geosci. Remote.*, 57, 8095-8104, doi: 10.1109/TGRS.2019.2918301,
564 2019.
- 565
- 566 Liu, J., Huang, J., Chen, B., Zhou, T., Yan, H., Jin, H., Huang, Z., and Zhang B.: Comparisons of PBL heights derived from
567 CALIPSO and ECMWF reanalysis data over China, *J. Quant. Spectrosc. Ra.*, 153, 102–112, doi: 10.1016/j.jqsrt.2014.10.011,
568 2015.
- 569
- 570 Manninen, A. J., Marke, T., Tuononen, M. J., and O'Connor, E. J.: Atmospheric boundary layer classification with Doppler
571 lidar, *J. Geophys. Res. Atmos.*, 123, 8172–8189, doi:10.1029/2017JD028169, 2018.
- 572
- 573 Martucci, G., Matthey, R., Mitev, V., and Richner, H.: Comparison between backscatter lidar and radiosonde measurements
574 of the diurnal and nocturnal stratification in the lower troposphere, *J. Atmos. Oceanic Technol.*, 24, 1231-1244,
575 doi:10.1175/JTECH2036.1, 2007.
- 576
- 577 Menut, L., Flamant, C., Pelon, J., and Flamant, P. H.: Urban boundary layer height determination from lidar measurements
578 over the Paris area, *Appl. Opt.*, 38, 945-954, doi:10.1364/AO.38.000945, 1999.
- 579



- 580 Morille, Y., Haeffelin, M., Drobinski, P., and Pelon, J.: STRAT: An automated algorithm to retrieve the vertical structure of
581 the atmosphere from single-channel lidar data, *J. Atmos. Oceanic Technol.*, 24, 761-775, doi:10.1175/JTECH2008.1, 2007.
582
- 583 Newsom, R. K., Turner, D. D., Mielke, B., Clayton, M., Ferrare, R., and Sivaraman, C.: Simultaneous analog and photon
584 counting detection for Raman lidar, *Appl. Opt.*, 48, 3903–3914, doi:10.1364/AO.48.003903, 2009.
585
- 586 Nieuwstadt, F. T .M. and Brost, R. A.: The decay of convective turbulence, *J. Atmos. Sci.*, 43, 532-546, doi:10.1175/1520-
587 0469(1986)0432.0.CO;2, 1986.
588
- 589 Pal, S., Behrendt, A., and Wulfmeyer, V.: Elastic-backscatter-lidar-based characterization of the convective boundary layer
590 and investigation of related statistics, *Ann. Geophys.*, 28, 825–847, doi:10.5194/angeo-28-825-2010, 2010.
591
- 592 Pal, S., Haeffelin, M., and Batchvarova, E.: Exploring a geophysical process-based attribution technique for the
593 determination of the atmospheric boundary layer depth using aerosol lidar and near-surface meteorological measurements, *J.*
594 *Geophys. Res. Atmos.*, 118, 9277-9295, doi:10.1002/jgrd.50710, 2013.
595
- 596 Pal, S., Lopez, M., Schmidt, M., Ramonet, M., Gibert, F., Xueref-Remy, I., and Ciais, P: Investigation of the atmospheric
597 boundary layer depth variability and its impact on the ²²²Rn concentration at a rural site in France, *J. Geophys. Res. Atmos.*,
598 120, 623–643, doi:10.1002/2014JD022322, 2015.
599
- 600 Sawyer, V. and Li, Z.: Detection, variations and intercomparison of the planetary boundary layer depth from radiosonde,
601 lidar and infrared spectrometer, *Atmos. Environ.*, 79, 518-528, doi:10.1016/j.atmosenv.2013.07.019, 2013.
602
- 603 Seibert, P., Beyrich, F., Gryning, S. E., Joffre, S., Rasmussen, A., and Tercier, P.: Review and intercomparison of
604 operational methods for the determination of the mixing height, *Atmos. Environ.*, 34, 1001–1027, doi:10.1016/S1352-
605 2310(99)00349-0, 2000.
606
- 607 Seidel, D. J., Ao, C. O., and Li, K.: Estimating climatological planetary boundary layer heights from radiosonde observations:
608 Comparison of methods and uncertainty analysis, *J. Geophys. Res.*, 115, D16113, doi:10.1029/2009JD013680, 2010.
609
- 610 Stull, R. B.: *An Introduction to Boundary Layer Meteorology*, Kluwer Acad. Publ., Netherlands, 1988.
611



- 612 Su, T., Li, J., Li, C., Xiang, P., Lau, K. H., Guo, J., et al.: An intercomparison of long-term planetary boundary layer heights
613 retrieved from CALIPSO, ground-based lidar, and radiosonde measurements over Hong Kong, *J. Geophys. Res. Atmos.*,
614 122, 3929–3943, doi:10.1002/2016JD025937, 2017.
- 615
- 616 Su, T., Li, Z., and Kahn, R.: Relationships between the planetary boundary layer height and surface pollutants derived from
617 lidar observations over China: regional pattern and influencing factors, *Atmos. Chem. Phys.*, 18, 15921–15935,
618 doi:10.5194/acp-18-15921-2018, 2018.
- 619
- 620 Su, T., Li, Z., and Kahn, R.: A new method to retrieve the diurnal variability of planetary boundary layer height from lidar
621 under different thermodynamic stability conditions, *Remote Sensing of Environment*, 237, 111519,
622 doi:10.1016/j.rse.2019.111519, 2020.
- 623
- 624 Wang, Z., Liu, D., Zhou, J., and Wang, Y.: Experimental determination of the calibration factor of polarization-Mie lidar,
625 *Opt. Rev.*, 16, 566-570, doi:10.1007/s10043-009-0111-7, 2009.
- 626
- 627 Wilde, N. P., Stull, R. B., and Eloranta, E. W.: The LCL Zone and Cumulus Onset, *J. Clim. Appl. Meteorol.*, 24, 640-657,
628 doi:10.1175/1520-0450(1985)0242.0.CO;2, 1985.
- 629
- 630 Wulfmeyer, V.: Investigation of turbulent processes in the lower troposphere with water-vapor DIAL and radar-RASS, *J.*
631 *Atmos. Sci.*, 56, 1055-1076, doi:10.1175/1520-0469(1999)0562.0.CO;2, 1999.
- 632
- 633 Wulfmeyer, V., Pal, S., Turner, D., and Wagner, E.: Can water vapor Raman lidar resolve profiles of turbulent variables in
634 the convective boundary layer?, *Boundary-Layer Meteorol.*, 136, 253-284, doi:10.1007/s10546-010-9494-z, 2010.
- 635
- 636 Zhang, W., Guo, J., Miao, Y., Liu, H., Zhang, Y., Li, Z., and Zhai, P.: Planetary boundary layer height from CALIOP
637 compared to radiosonde over China, *Atmos. Chem. Phys.*, 16, 9951–9963, doi:10.5194/acp-16-9951-2016, 2016.
- 638
- 639 Zhang, Y., Seidel, D. J., and Zhang, S.: Trends in planetary boundary layer height over Europe, *J. Clim.*, 26, 10,071–10,076,
640 doi:10.1175/JCLI-D-13-00108.1, 2013.
- 641
- 642 Zhang, Y., Yi, F., Kong, W., and Yi, Y.: Slope characterization in combining analog and photon count data from
643 atmospheric lidar measurements, *Appl. Opt.*, 53, 7312-7320, doi:10.1364/AO.53.007312, 2014.
- 644



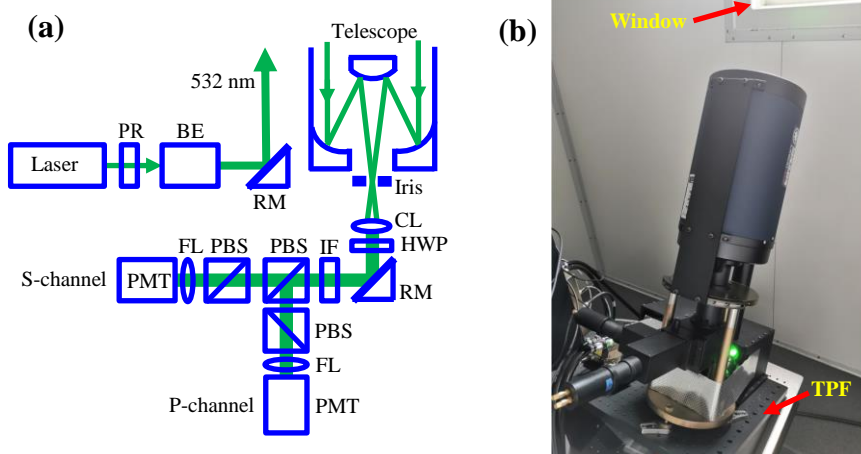
645 Zhu, X., Tang, G., Guo, J., Hu, B., Song, T., Wang, L., Xin, J., Gao, W., Münkler, C., Schäfer, K., Li, X., and Wang, Y.:
646 Mixing layer height on the North China Plain and meteorological evidence of serious air pollution in southern Hebei, Atmos.
647 Chem. Phys., 18, 4897–4910, doi: 10.5194/acp-18-4897-2018, 2018.

648
649
650
651
652
653
654
655
656
657
658
659
660
661
662
663
664
665
666
667
668
669
670
671
672
673
674
675
676
677
678



679

680



681

682

683 **Figure 1: (a) Schematic optical layout of the TPL. PR, polarizer; BE, beam expander; RM, reflecting mirror; CL,**
684 **collimating lens; HWP, half-wavelength plate; IF, interference filter; PBS, polarization beam splitter; FL, focusing**
685 **lens; PMT, photomultiplier tube; (b) a picture of the lidar optics. The whole optics is placed on a tilted platform**
686 **(TPF). A window permits propagating laser beam and atmospheric backscatter to pass through without blocking.**

687

688

689

690

691

692

693

694

695

696

697

698

699

700

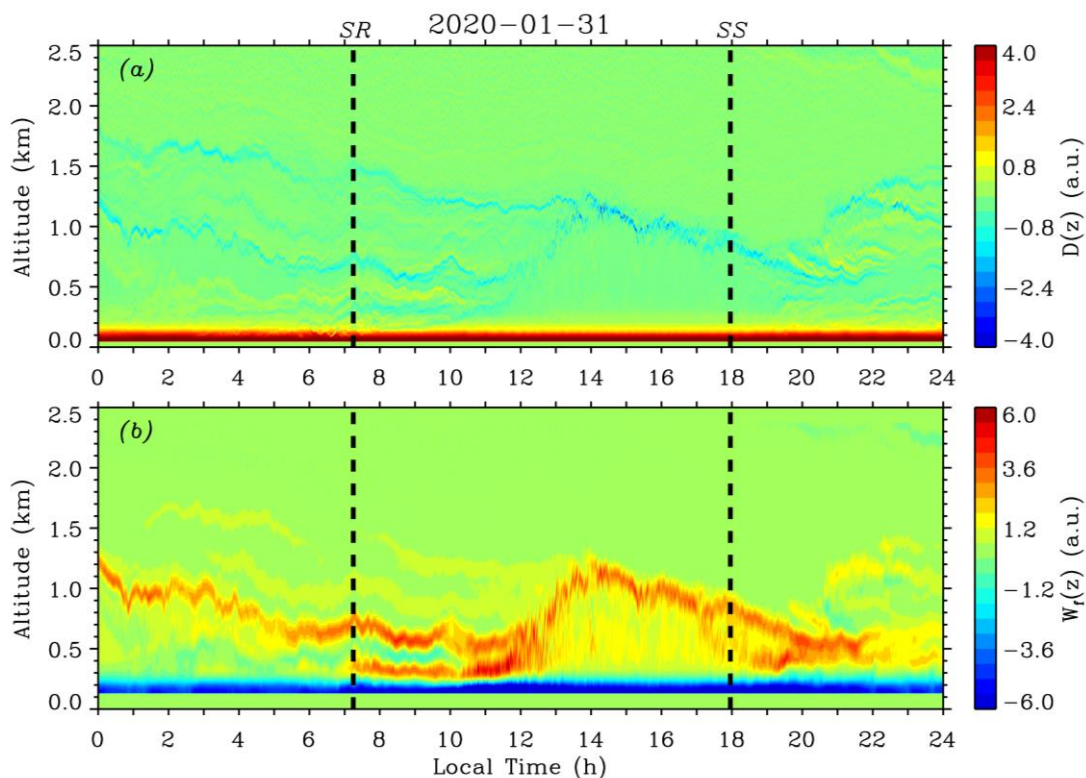
701

702



703

704



705

706

707 **Figure 2: Contour plots of (a) $D(z)$ and (b) $W_f(z)$ on Jan 31, 2020. Sunrise (SR) and sunset (SS) times are marked by**
708 **thick black dashed lines. Multiple (residual) aerosol layers which definitely lead to misattribution of ABL depth, are**
709 **clearly indicated by stripes of local minima of $D(z)$ and maxima of $W_f(z)$ in the contour plots. By visualizing these**
710 **contour plots, proper upper heights for applying the variance method can be conveniently and correctly determined**
711 **to be below the base of multiple (residual) aerosol layers aloft.**

712

713

714

715

716

717

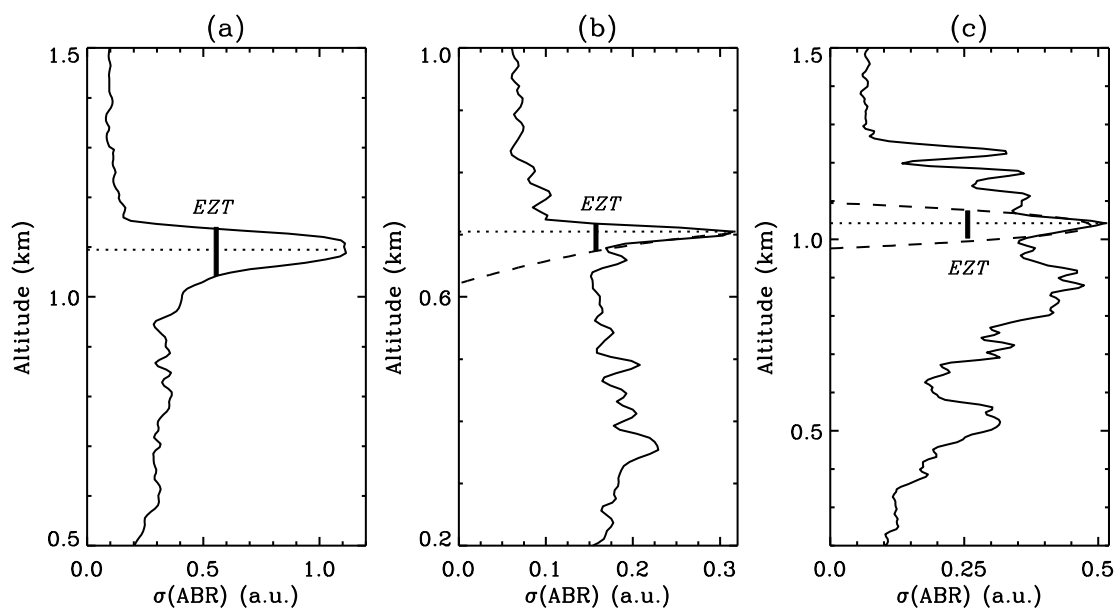
718

719



720

721



722

723

724

725

726

727

728

729

730

731

732

733

734

735

736

737

738

739

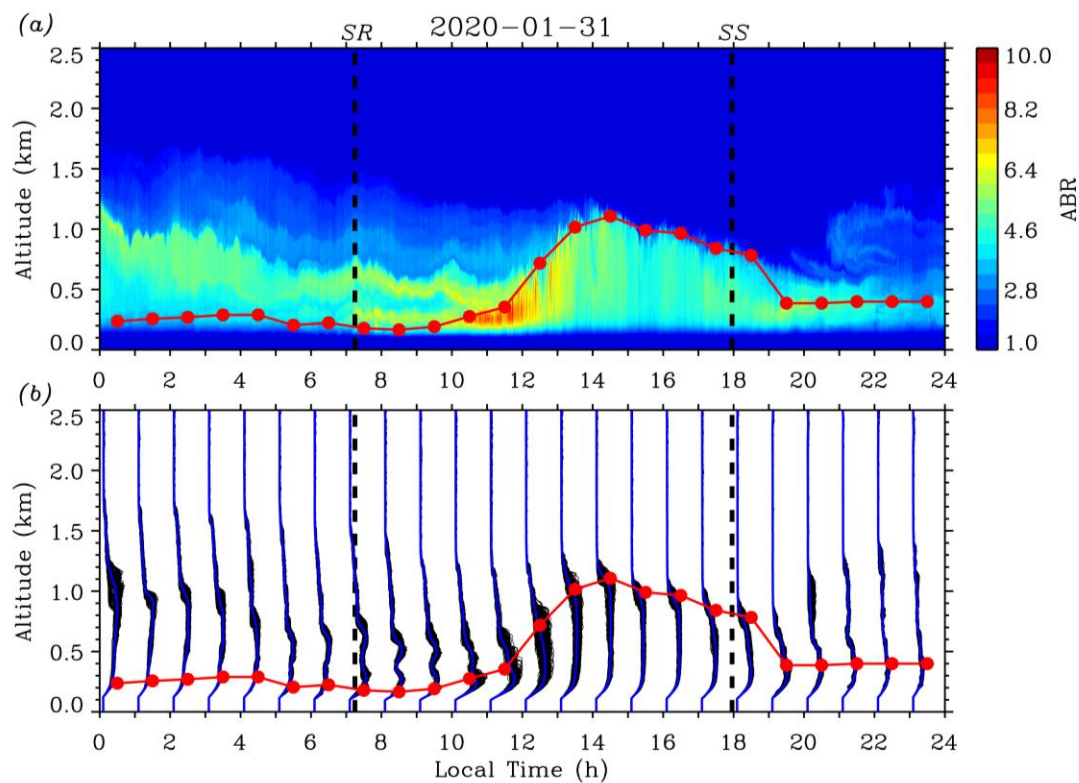
740

Figure 3: Illustrations of the FWHM method using the variance of ABR fluctuations to determine the CBL depth and subsequent EZT. Thin black lines indicate the standard deviation of ABR fluctuations, $\sigma(\text{ABR})$. Thin dotted lines specify the CBL depth with maximum $\sigma(\text{ABR})$. Thick vertical lines represent the determined EZT (EZ). (a) For a strong updraft case, both the upper and lower edges near the peak $\sigma(\text{ABR})$ are clear-cut and steep. The EZT can be directly obtained; (b) for a less-intense updraft case, the lower edge is not clear-cut enough. A quadratic polynomial fitting (dashed line) is applied to the lower edge to help determine the EZT; (c) for a weak turbulence and advected aerosol case, neither the upper nor the lower edge is clear-cut enough. Quadratic polynomial fittings (dashed lines) are applied to both edges to help determine the EZT.



741

742



743

744

745 **Figure 4: (a) Contour plot of the ABR on Jan 31, 2020; (b) over-plots of ABR profiles (thin black lines) in each 1-h**
746 **time interval and the hourly mean ABR profile (blue line). SR and SS times are indicated by thick black dashed lines.**
747 **Red solid circle represents the hourly mean ABL depth retrieved by the variance method and the red line indicates**
748 **the diurnal evolution trend of the ABL depth.**

749

750

751

752

753

754

755

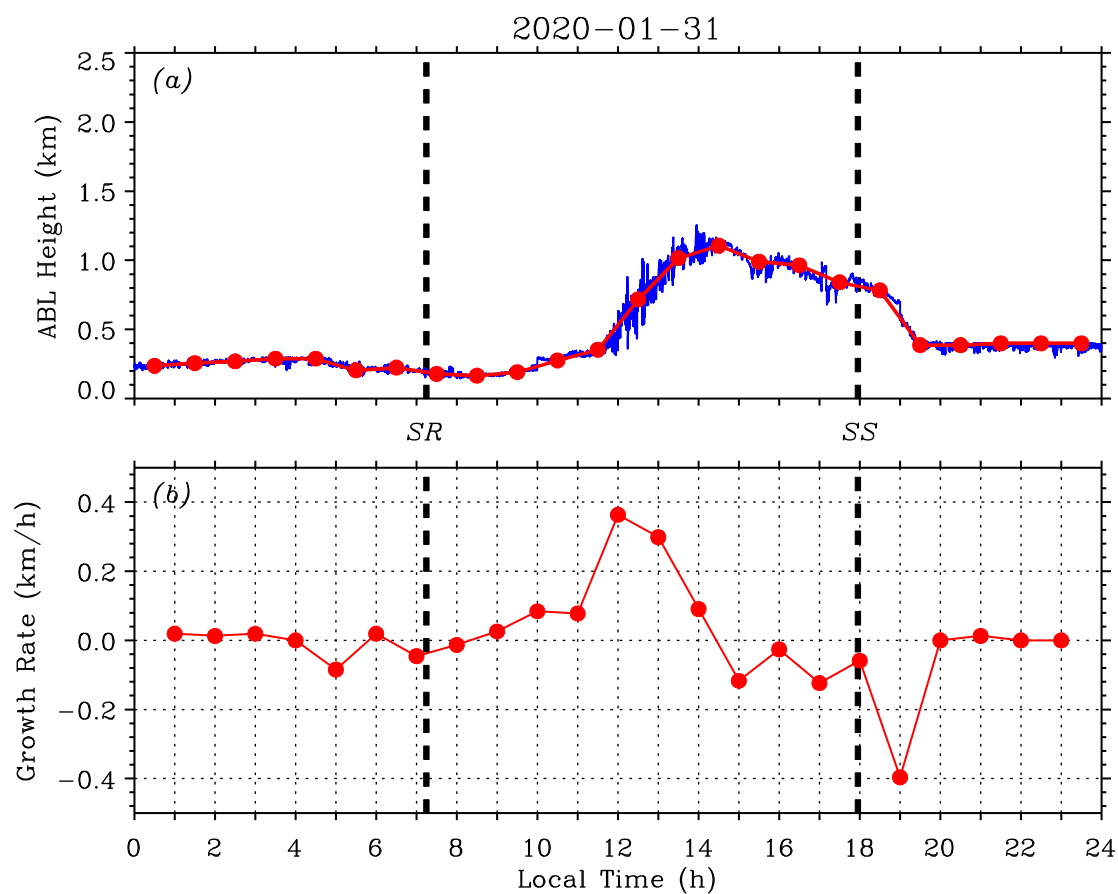
756

757



758

759



760

761

762 **Figure 5: (a) instantaneous ABL depths (blue) obtained by LGM method (before 1000 and after 1900 LT) and HWT**
763 **method (between 1000 and 1900 LT). Red solid circles indicate the hourly mean ABL depth by variance method; (b)**
764 **hourly mean ABL depth growth rate. Thick black dashed lines mark the SR and SS times on Jan 31, 2020.**

765

766

767

768

769

770

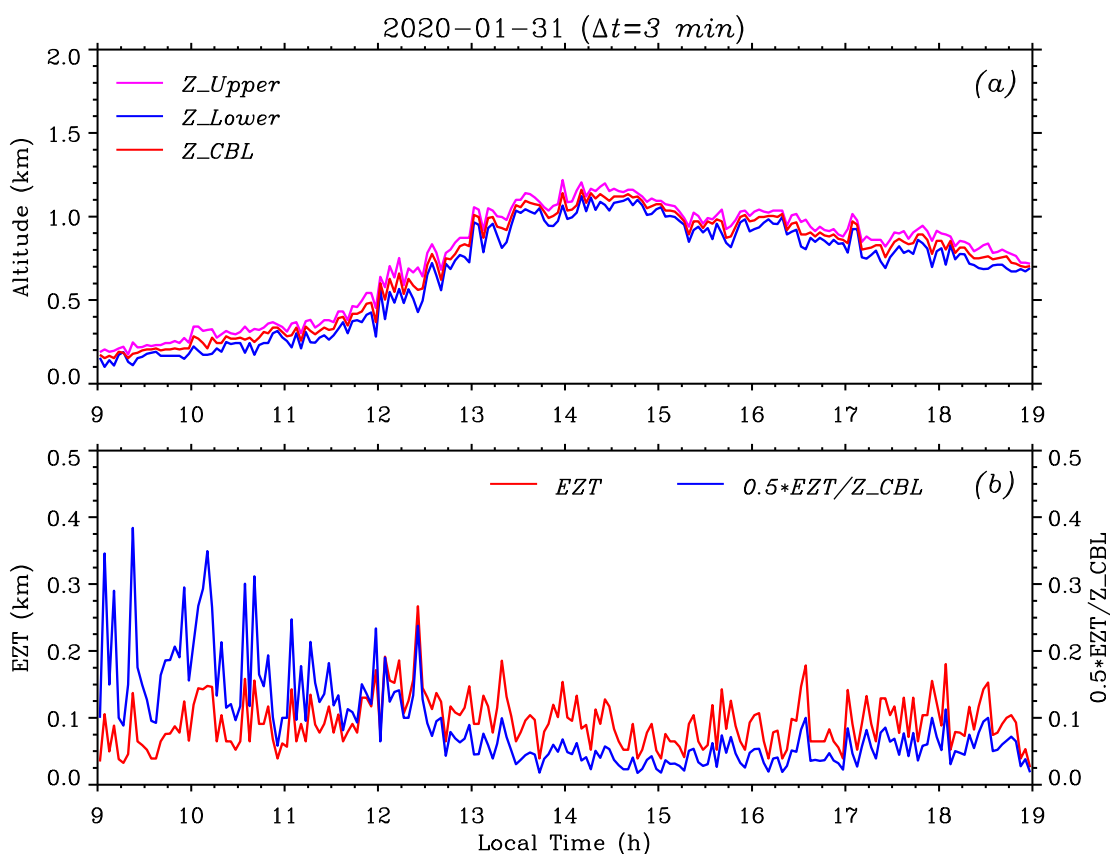
771

772



773

774



775

776

777 **Figure 6: (a) The CBL depth Z_{CBL} (red) obtained by the variance method between 0900 and 1900 LT on Jan 31,**
778 **2020. The EZ upper height Z_{Upper} (magenta) and lower height Z_{Lower} (blue) are derived from the FWHM of the**
779 **$\sigma(\text{ABR})$ profile each of which is calculated within a time interval of 3 min; (b) corresponding EZT (red) and ratio of**
780 **EZT to Z_{CBL} (blue) during the same time interval. Note the ratio is multiplied by a factor of 0.5 so that the two**
781 **vertical axes share the same scaling range.**

782

783

784

785

786

787

788



789
 790
 791

Table 1: Statistics of EZT obtained on Jan 31, 2020

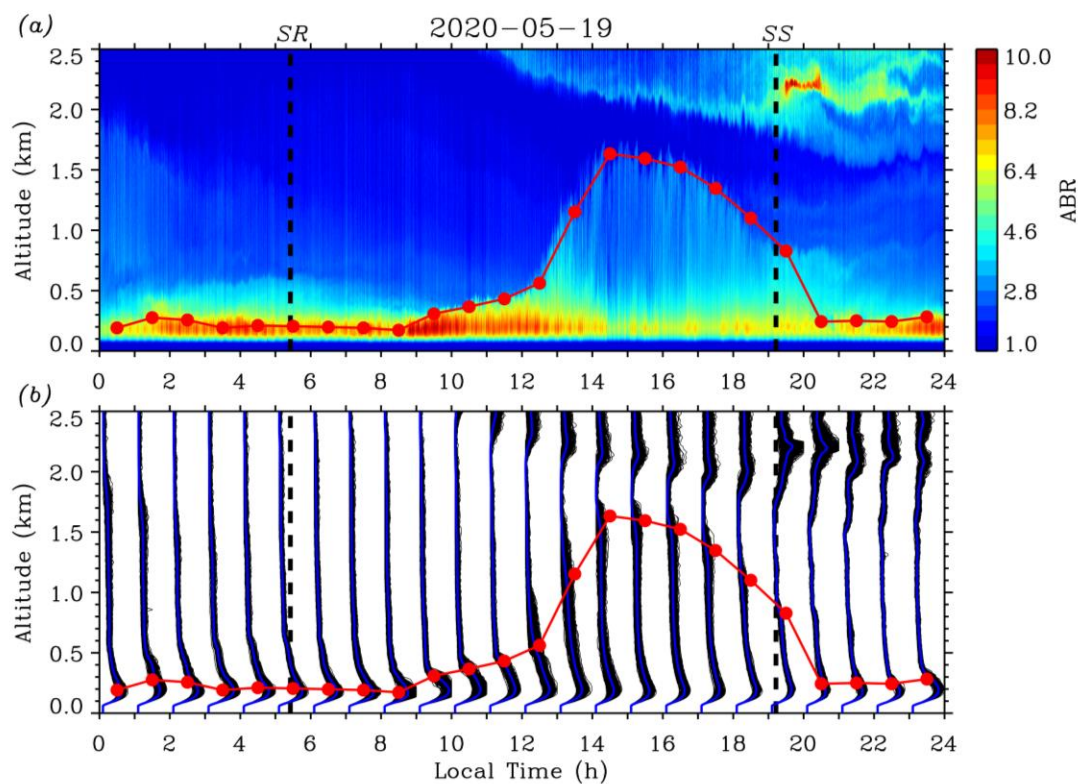
Stage of CBL	Formation	Growth	Quasi-stationary	Decay	Total	
Time Interval (LT)	0900-1130	1130-1330	1330-1630	1630-1900	0900-1900	
Statistical data of EZT(km)	<i>min</i>	0.033	0.065	0.039	0.026	0.026
	<i>max</i>	0.158	0.267	0.154	0.180	0.267
	<i>mean</i>	0.085	0.122	0.082	0.095	0.094
	<i>stddev</i>	0.036	0.041	0.028	0.036	0.038
Percentages in each EZT subrange (%)	0.00-0.05 km	16.0	0.0	10.0	6.0	8.5
	0.05-0.10 km	54.0	27.5	65.0	52.0	51.5
	0.10-0.15 km	26.0	52.5	23.3	34.0	32.5
	0.15-0.20 km	4.0	17.5	1.7	8.0	7.0
	0.20-0.30 km	0.0	2.5	0.0	0.0	0.5

792
 793
 794
 795
 796
 797
 798
 799
 800
 801
 802
 803
 804
 805



806

807



808

809

810 **Figure 7: Same as Figure 4 but on the day of May 19, 2020.**

811

812

813

814

815

816

817

818

819

820

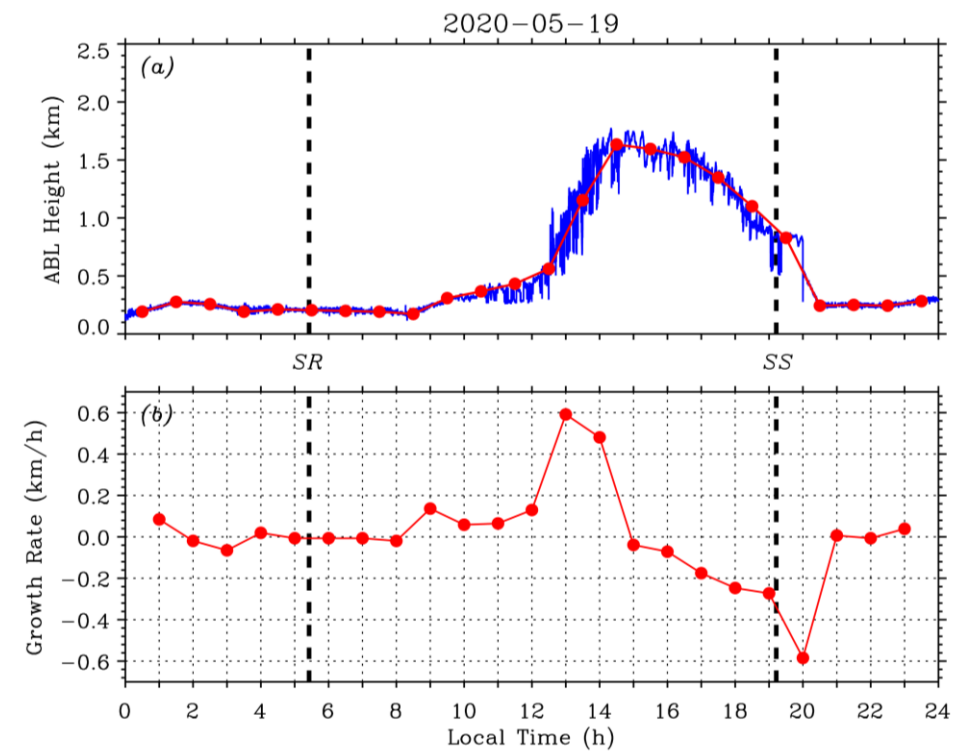
821

822



823

824



825

826

827 **Figure 8: Same as Figure 5 but on the day of May 19, 2020.**

828

829

830

831

832

833

834

835

836

837

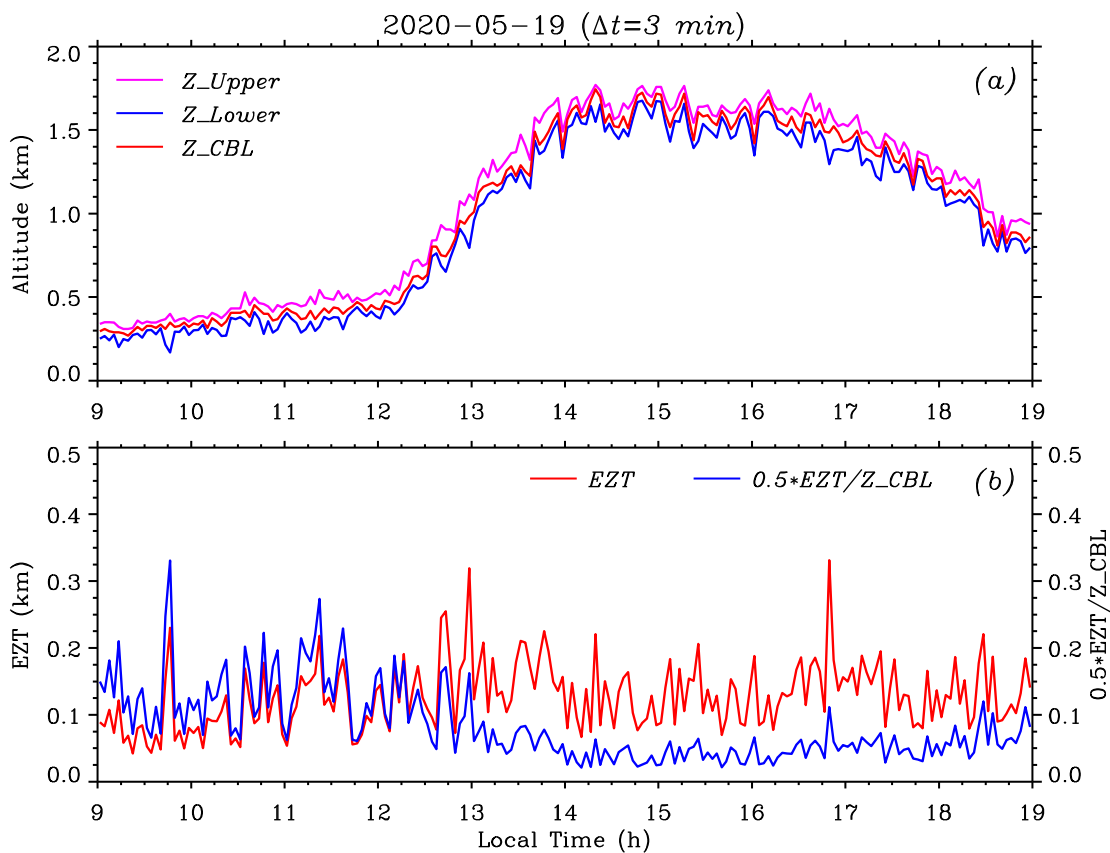
838

839

840



841
842



843
844
845
846
847
848
849
850
851
852
853
854
855
856

Figure 9: Same as Figure 6 but on the day of May 19, 2020.



857

858

859

Table 2: Statistics of EZT obtained on May 19, 2020

Stage of CBL		Formation	Growth	Quasi-stationary	Decay	Total
Time Span (LT)		0900-1230	1230-1430	1430-1630	1630-1900	0900-1900
Statistical data of EZT(km)	<i>min</i>	0.042	0.066	0.070	0.079	0.042
	<i>max</i>	0.230	0.319	0.206	0.331	0.331
	<i>mean</i>	0.106	0.153	0.122	0.142	0.127
	<i>stddev</i>	0.044	0.057	0.035	0.046	0.049
Percentages in each EZT subrange (%)	0.00-0.05 km	5.7	0	0	0	2.0
	0.05-0.10 km	50.0	20.0	35.0	20.0	33.5
	0.10-0.15 km	25.7	32.5	40.0	40.0	33.5
	0.15-0.20 km	15.7	27.5	22.5	36.0	24.5
	0.20-0.34 km	2.9	20.0	2.5	4.0	6.5

860

861

862

863

864

865

866

867

868

869

870

871

872

873



874

875

876

Table 3: Comparisons of EZT statistics for the winter and summer cases

Case 1 (Jan 31, 2020)		Formation	Growth	Quasi-stationary	Decay	Total
Time Span (LT)		0900-1130	1130-1330	1330-1630	1630-1900	0900-1900
Statistical data (km)	<i>mean</i>	0.085	0.122	0.082	0.095	0.094
	<i>stddev</i>	0.036	0.041	0.028	0.036	0.038
Percentages (%)	0.00-0.05 km	16.0	0.0	10.0	6.0	8.5
	0.05-0.15 km	80.0	80.0	88.3	86.0	84.0
	0.15-0.30 km	4.0	20.0	1.7	8.0	7.5
Case 2 (May 19, 2020)		Formation	Growth	Quasi-stationary	Decay	Total
Time Span (LT)		0900-1230	1230-1430	1430-1630	1630-1900	0900-1900
Statistical data (km)	<i>mean</i>	0.106	0.153	0.122	0.142	0.127
	<i>stddev</i>	0.044	0.057	0.035	0.046	0.049
Percentages (%)	0.00-0.05 km	5.7	0	0	0	2.0
	0.05-0.15 km	75.7	52.5	75.0	60.0	67.0
	0.15-0.34 km	18.6	47.5	25.0	40.0	31.0

877

878